Journal of the European Ceramic Society 44 (2024) 5347–5357

Contents lists available at ScienceDirect

Journal of the European Ceramic Society

journal homepage: www.elsevier.com/locate/jeurceramsoc

Local indentation response of carbon fibers embedded in a harsh environment: The sintered ultra-high temperature ceramic matrix

Pietro Galizia *, Simone Failla, Cesare Melandri, Diletta Sciti

National Research Council of Italy - Institute of Science, Technology and Sustainability for Ceramics (CNR - ISSMC; former ISTEC), Via Granarolo 64, 48018 Faenza, Italy

ARTICLE INFO

Keywords:
Ceramic matrix composites (CMCs)
Ultra-high temperature ceramics (UHTC)
Hardness
Indentation
Pitch carbon fiber

ABSTRACT

Understanding the properties of the constituent elements within Ceramic Matrix Composites (CMCs) is of paramount importance. During manufacturing process, the properties of the starting phases can undergo changes or be influenced by their interactions. In this work, micro-indentation analysis was used to selectively characterize matrix and fiber of Ultra-High-Temperature CMCs (UHTCMCs) produced by slurry infiltration of unidirectional pitch-derived carbon fabrics and sintering. A loading pre-factor was exploited to differentiate between indentations made on the matrix and those made on the fibers. The ZrB_2-based matrix showed typical elasto-plastic behavior, leaving a residual imprint, with hardness and a modulus of 11.5 GPa and 220 GPa, respectively, consistent with its porosity, cracks and fiber content. Conversely, the fiber displayed no residual imprint and displayed hardness and modulus values of 1.1 GPa and 40 GPa, respectively. These values were attributed to the graphitic sheets buckling and residual thermal stress. Furthermore, the indentations indicated a transition zone between the matrix and fiber affecting mechanical behavior.

1. Introduction

Ultra-High-Temperature Ceramic Matrix Composites (UHTCMCs) are a novel class of ultra-refractory materials that can support the demand of structural materials to be used in harsh environments [1–6]. Research and focus on this material class began gaining significant momentum in the early 2000s [7]. However, it is noteworthy that since 2015, there has been a substantial acceleration in the interest and development of these materials [8–11]. Among the various manufacturing processes, typically based on chemical vapor infiltration [12–15], polymer infiltration and pyrolysis [16–19], sintering [20–25], or reactive melt infiltration [26–29], research at CNR (the National Research Council of Italy) on UHTCMCs has primarily focused on the development of ZrB_2-based matrices reinforced with pitch-derived carbon fibers using hot pressing or spark plasma sintering [30]. Major breakthroughs were achieved within the Horizon 2020 European research project entitled 'Next Generation Ceramic Composites for Harsh Combustion Environment and Space (C^3HARME)' [31]. In this specific subcategory of UHTCMCs, a superior trade-off between oxidation/ablation resistance and structural properties was demonstrated compared to others [32–34]. This accomplishment can be attributed to distinctive microstructural features, including a dense UTHC matrix and the use of high modulus pitch-derived fiber without coating. These features facilitate efficient matrix/fiber stress transfer and toughening mechanisms, such as intra-fiber pull-in, owing to the layered structure of the selected fiber [35]. Moreover, the utilization of the sintering process and bare carbon fiber reduces both time and processing cost while achieving better fiber distribution within the matrix. In fact, for coated fibers, less than 15 % of the total fiber amount dispersed into the matrix as individual filaments; whereas in the case of uncoated fibers, as much as 40 % of the fibers were dispersed into the matrix as individual filaments [36]. However, this choice resulted in jagged matrix/fiber interfaces and high levels of thermal residual stress approaching 600 MPa tensile stress within the matrix [36–38]. Sauder et al. showed that pitch-derived carbon fibers, when stretched at high temperatures, exhibit a decrease in Young's modulus and an increase in tensile strength, at least up to 2400 °C [39]. However, they presented the stress-strain behavior of the fibers at room temperature neither after a thermal cycle, nor after a thermal cycle with transverse loading, such as that imposed during pressure-assisted sintering. Although some degradation of the fiber mechanical properties cannot be ruled out, the bending strength and toughness properties remain comparable to those

* Corresponding author.
E-mail address: pietro.galizia@cnr.it (P. Galizia).

https://doi.org/10.1016/j.jeurceramsoc.2023.12.025
Received 14 September 2023; Received in revised form 22 November 2023; Accepted 6 December 2023
Available online 10 December 2023

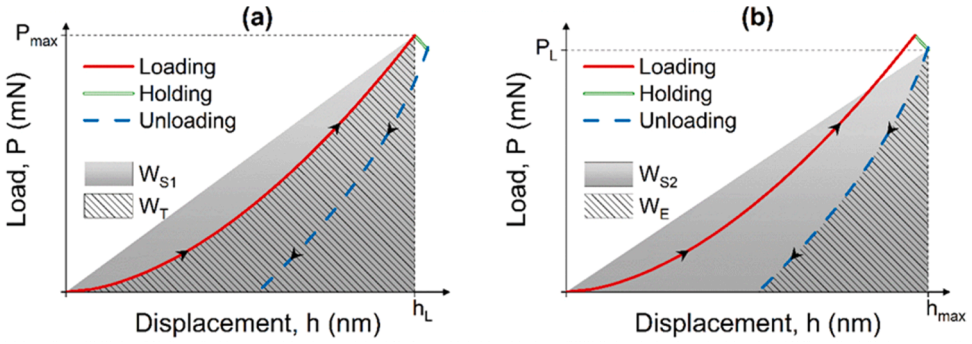

Fig. 1. Illustration of typical load-displacement curves obtained from indentation. The shaded areas are those used to calculate (a) total energy constant ($\nu_T = W_{S1}/W_T$); and (b) elastic energy constant ($\nu_E = W_{S2}/W_E$).

of the same composite reinforced with coated fibers [40]. Furthermore, supporting the absence of degradation in fiber mechanical properties, after sintering process, observations revealed that (i) the distribution of fiber diameter of sintered composites remained unchanged [36] and (ii) the composite's overall coefficient of thermal dilation gradually approached that of bare carbon fiber as the matrix was progressively damaged [36–38].

In the field of fiber-reinforced composites, the indentation technique is commonly used to in situ assess the interfacial shear strength [41]. This technique is generally used for polymer matrix composites [42], and ceramic matrix composites where debonding and fiber splitting can occur under the testing conditions [43,44]. In case of a strong fiber-matrix interface, such as jagged C_f/ZrB_2 interfaces, inducing fiber push-out can be challenging due to the tendency of graphite sheets to bend, buckle, or simply spread under the indenter tip [45–47]. Notably, despite the occurrence of buckling of graphene sheets and plastic sliding of graphite basal planes during indentation, experimental values of indentation modulus and hardness for pitch-derived carbon fiber have been estimated at approximately 80–100 GPa and 7 GPa, respectively [46–49]. As for the matrix, comprehensive indentation characterization of ZrB_2 is well-documented in the literature, with hardness values ranging from about 30–40 GPa, depending on lattice orientation and indentation modulus in the range of 550–700 GPa [50–56].

In this work, to further explore the mechanical behavior of the ZrB_2-based matrix and pitch-derived carbon fiber (C_f), as well as their mechanical interaction within sintered UHTCMCs, a micro-indentation campaign was conducted. This investigation enabled the evaluation of the hardness and indentation modulus of the individual components, providing insights into, the transition zone between fiber and matrix. It also shed light on the state of the carbon fiber after matrix sintering that can damage the fiber, forming the jagged interfaces. These newly formed interfaces create a "harsh environment" potentially acting as a source of mechanical stress for the fibers. Furthermore, the full densification of the matrix enhances this "harsh environment" due to a thermal expansion coefficient mismatch that exceeds $5 \bullet 10^{-6}$ °C^{-1} with the fiber along its longitudinal direction. This results in the fiber being in a compressed state when the composite is cooled down to room temperature after the sintering step [36]. Additionally, work-of-indentation values were calculated in agreement with Attaf [61] to correlate energies involved during the indentation tests with micromechanics phenomena.

2. Experimental

UHTCMCs based on unidirectional carbon fiber-reinforced ZrB_2 were produced through hot pressing at 1900 °C and 40 MPa. The final microstructure consisted in 55 vol% of matrix (composition: 83–84 vol% ZrB_2 + 9–10 vol% SiC/SiCN/BN + 6–7 vol% porosity) and 45 vol% of pitch-derived carbon fiber, C_f (XN80–6K, Granoc, Japan). Further details regarding slurry preparation, infiltration, densification, and microstructural and mechanical characteristic of the produced material can be found in previously published works [37,38,57,58].

Microstructures were analyzed with Field-Emission Scanning Electron Microscopy (FESEM, mod. ΣigmaCarl Zeiss NTS Gmbh Öberkochen, Germany) coupled with energy dispersive X-ray spectroscopy (mod. INCA energy 300; Oxford instruments, High Wycombe, UK). Grain size data were collected through image analysis on SEM images of polished cross section. The data were then fitted using the following Cumulative Distribution Function (CDF) function:

$$CDF = \frac{1}{1 + e^{\frac{x - D_{50}}{dx}}} \tag{1}$$

Where D_{50} is the corresponding median value (50th percentile) and dx is a constant that inversely affects the slope of the curve around D_{50} (the inflection point). The grain size density distribution was obtained as the first derivative of the fitted CDF.

Micro-indentation tests were performed with the Agilent MTS Nanoindenter XP. An array of 50 imprints was made with a Berkovich pyramidal diamond tip on a polished specimen down to 0.25 μm. The testing procedure was conducted under the following nominal conditions: a maximum load of 100 mN, a loading rate of 2 μN/min, no pause duration, and an unloading rate of 300 μN/min. The results of micro-indentation tests, such as the contact stiffness (S), indentation testing hardness (H), indentation modulus (M), were obtained using the Oliver & Pharr method [59,60]. Due to the expected anisotropy of UHTC matrix and the anisotropic nature of carbon fibers, the isotropic Poisson's ratio was not used. Instead, M was derived from the calculated effective modulus data (E_{eff}) using the following equation [53]:

$$E_{eff} = \frac{\sqrt{\pi} S}{2\sqrt{A}} \tag{2}$$

$$\frac{1}{M} = \frac{1}{E_{eff}} - \frac{1 - \nu_i^2}{E_i} \tag{3}$$

where S is the stiffness, A is the contact area, and $E_i = 1140$ GPa and $\nu_i = 0.07$ are the Young's modulus and Poisson's ratio of the diamond tip, respectively.

We chose microindentation up to 100 mN instead of nanoindentation to obtain hardness and modulus values representative of the entire ZrB_2-SiC matrix, including defects like pores, cracks, and the presence of fibres. This method differs from the focus on individual phases of ZrB_2 and SiC, intending to give homogenized values for both the matrix and fibres, considering the boundary conditions imposed by the composite structure.

The loading pre-factor (C), which describes the parabolic nature of the loading curve $P = Ch^2$, was calculated by fitting the experimental data for penetration depths between 80 and 150 nm [46].

Work-of-indentation values were calculated in agreement with Attaf [61]. Due to the relaxation phenomena that can occur between the end of loading step and the beginning of unloading step, the total and elastic

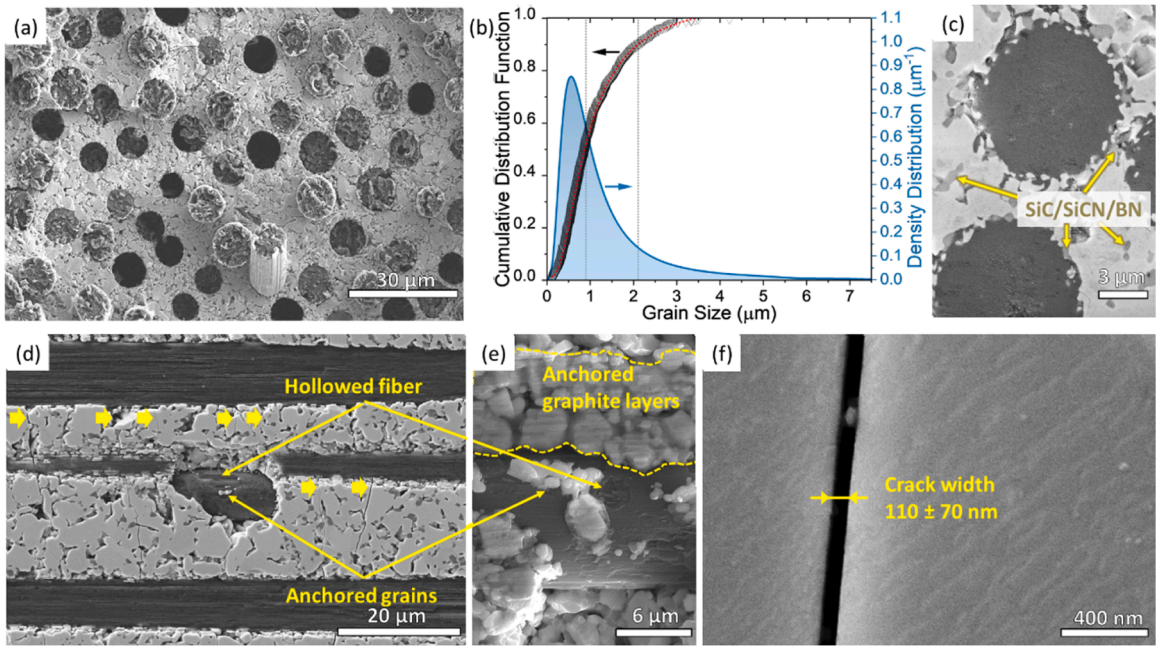

Fig. 2. (a) SEM image of fracture surface and (b) cumulative curve and density distribution of grain size. The cumulative curve is fitted by the equation: $1/\left(1+e^{\frac{x-0.94\mu m}{0.36\mu m}}\right)$. SEM images of (c) polished cross section with out-of-plane fiber, and (d) polished cross section and (e) fracture surface with in-plane fiber. The thick arrows point the presence of cracks in the matrix. (f) Zoom of a transverse matrix crack.

energy constants (ν_T and ν_E, respectively) were calculated as follows [62]:

$$\nu_T = W_{S1}/W_T \tag{4}$$

$$\nu_E = W_{S2}/W_E \tag{5}$$

Where W_{S1} and W_{S2} are the fictitious absolute works done during to the loading and unloading curves, respectively (see Fig. 1), W_T is the total mechanical work done during loading step and W_E is the recovered elastic energy during unloading step. Referring to Fig. 1, the areas under the loading and unloading curves represent W_T and W_E, respectively, h_L denotes the penetration depth at which the increase in loading ceases, and P_L denotes the load value at which the increase in displacing ceases.

The distance between the center of indentation and the closest matrix/fiber interface (δ) and the grain size (d) were measured through image analysis (Image-Pro Analyzer 7.0, v.7, Media Cybernetics, USA) of FESEM images.

3. Results and discussion

3.1. Microstructural characterization

The microstructure obtained after densification is showed in Fig. 2. The dense microstructure consisted in ceramic grains between 0.4 µm (D_{10}) and 2.1 µm (D_{90}), and 45 vol% of well-dispersed fibers (Fig. 2a and b). In Fig. 2c, SiC/SiCN/BN phases appear as darker grains owing to

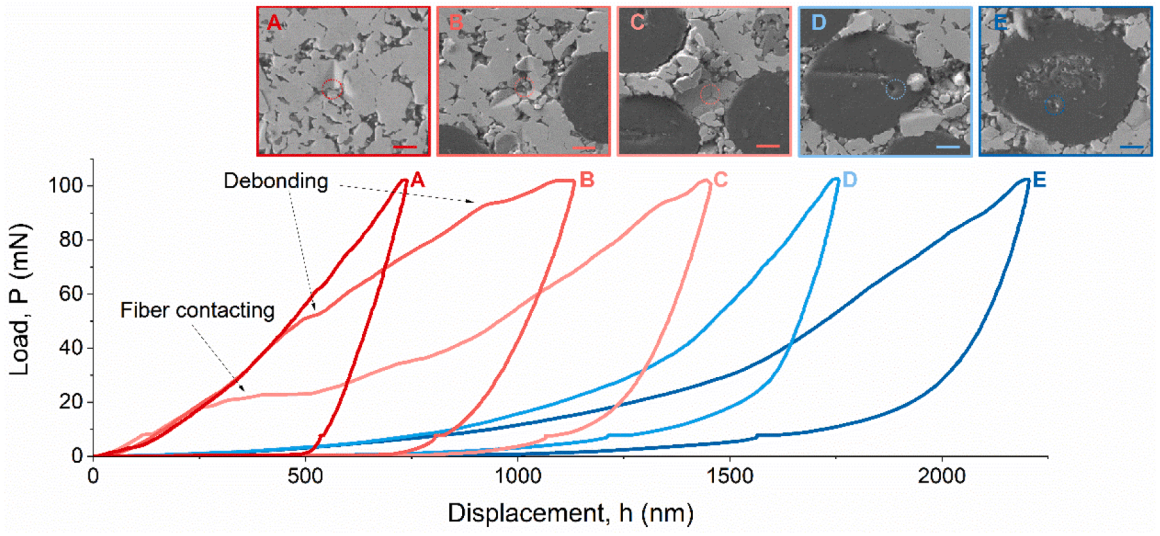

Fig. 3. Force (P) versus indentation depth (h) curves from micro-indentation tests at five representative points: (A) matrix, (B-D) matrix/fiber, and (E) fiber. Each curve is accompanied by a corresponding SEM image of the indentation imprint. In each image, a scale bar of 2 µm and a dotted circled marker indicating the centre of the indentation imprint are provided. The curves A-E correspond to the indentation number 9, 31, 22, 35 and 1, respectively (see Table A1).

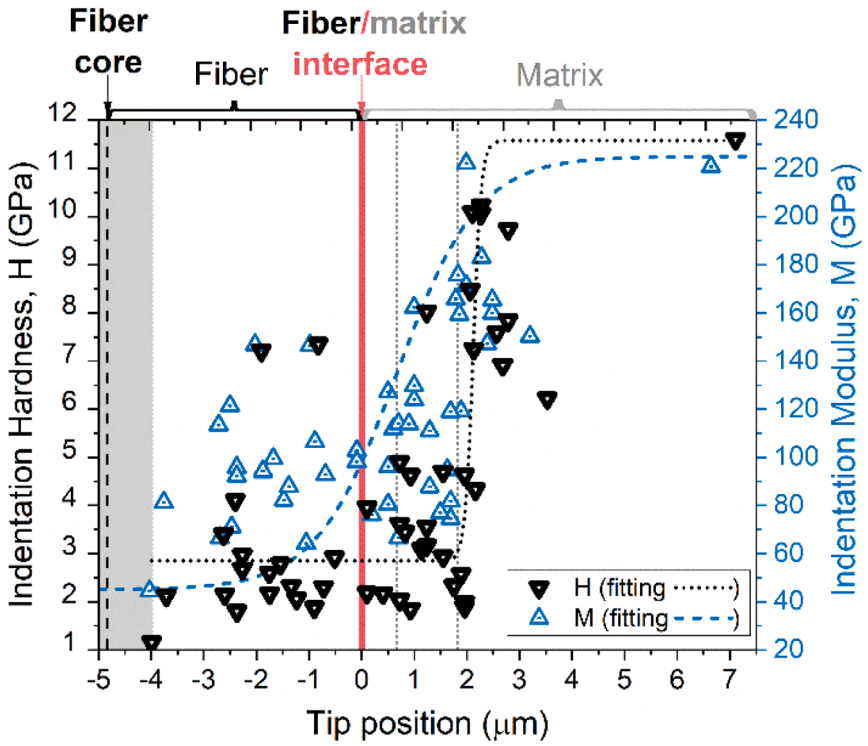

Fig. 4. Indentation hardness (H) and modulus (M) versus tip position with respect to the fiber/matrix interface (vertical red line at x = 0). The H-values are fitted by the equation: $11.6GPa + (2.8GPa - 11.6GPa)/\left(1 + e^{\frac{x-2.1\mu m}{0.1\mu m}}\right)$, while for M-values the equation: $45GPa + (225GPa - 45GPa)/\left(1 + e^{\frac{x-0.9\mu m}{0.8\mu m}}\right)$ is plotted. Vertical dotted lines at 0.9 μm (D_{50}) and 2.1 μm (D_{90}) highlight the range of cumulative percentile values (the size point below which 50 % and 90 % of the grains are contained) for reference.

their lower density compared to ZrB_2. Moreover, Fig. 2c showcases the distinctive jagged matrix/fiber interface of these sintered UHTCMCs. This strong matrix/fiber interface was formed as consequence of the ceramic matrix's sintering shrinkage [35] and chemical reactions between C and oxide phases present in the ZrB_2 particle surface, such as B_2O_3 and ZrO_2 [57]. These chemical reactions and matrix shrinkage hollowed the fibers and anchored the external layers of the carbon fibers to the matrix (see Fig. 2d and e). Indeed, the fracture surface (Fig. 2a and e) displays the characteristic mode of fracture for C_f, which tends to exfoliate [35,63]. The resulting fiber pull-out occurred through intra-fiber sliding, facilitated by the sliding of the graphite sheets, while the outer fiber layer remained firmly anchored to the matrix. Finally, Fig. 2d displays another typical microstructural feature of these sintered UHTCMCs: transverse matrix cracks spaced with a periodicity of about 25 μm [38]. These cracks, with a width of 110 ± 70 nm (Fig. 2f), were formed during the cooling step due to the coefficient thermal expansion mismatch, exceeding $5 \bullet 10^{-6} \circ C^{-1}$, between the matrix and the fiber along its longitudinal direction [37,38].

3.2. Micro-indentation characterization

3.2.1. Indentation curves

Fig. 3 displays representative load-displacement curves obtained through instrumented micro-indentation. The maximum indentation depth gradually increased, ranging from 740 nm for the indentations involving the matrix (curve A) to 2200 nm for those primarily engaging the fibers (curves D and E). These displacements correspond to imprints with a radius of 3–4 μm in the harder and stiffer UHTC matrix and contact imprints with a size up to 9.5 μm in the fibre sections. Hence, the indentation response of the matrix and fiber mutually influence each other. Notably, the pop-in events observed in the matrix/fiber curves were attributed to debonding phenomena, which contributed to the wide range of indentation responses observed. Consequently, a

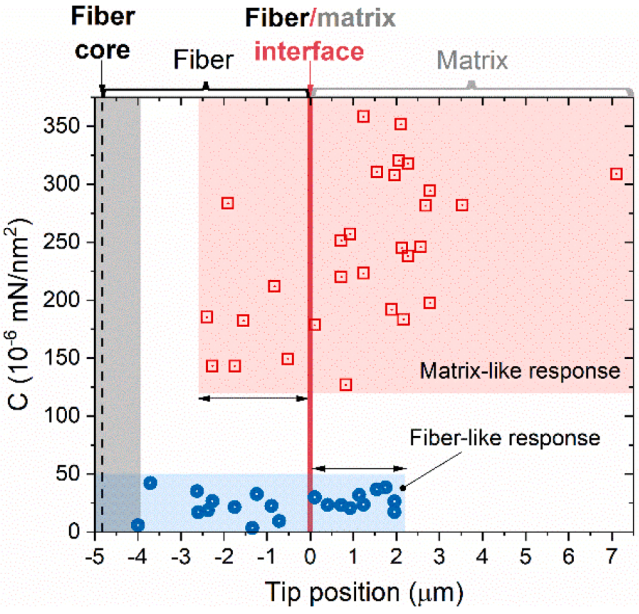

Fig. 5. Plot of loading pre-factor (C) versus tip position with respect to the fiber/matrix interface (vertical red line at x = 0).

significant dispersion exists in the calculated values of hardness (H), ranging from 1.2 GPa to 11.6 GPa, and modulus (M), ranging from 44 GPa to 222 GPa. These data for each curve are provided in Table A1.

3.2.2. Discerning fiber-like and matrix-like responses and transition zone

When plotting the hardness and modulus values as a function of the tip position relative to the fiber/matrix interface (see Fig. 4), a notable

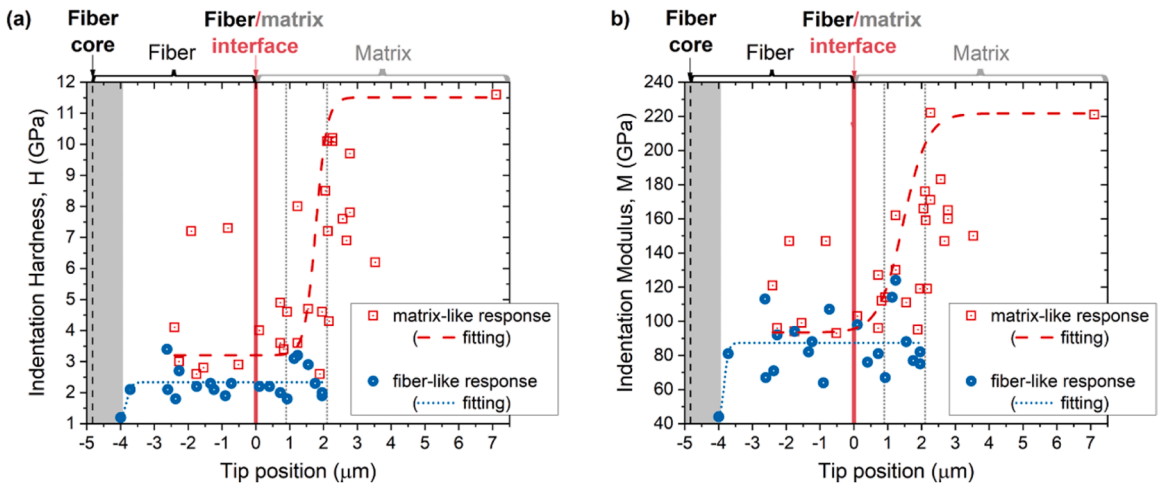

Fig. 6. (a) Indentation hardness (H) and (b) indentation modulus (M) versus tip position with respect to the fiber/matrix interface (vertical red line at x = 0). The indentation results were grouped in two different ensembles: matrix- like response (square symbols) and fiber-like response (circle symbols). The data is fitted by the following equations: $H_m = 11.5GPa + (3.2GPa - 11.5GPa)/\left(1 + e^{\frac{x-1.8\mu m}{0.2\mu m}}\right)$; $H_f = 2.3GPa + (1.1GPa - 2.3GPa)/\left(1 + e^{\frac{x+3.8\mu m}{0.1\mu m}}\right)$; $M_m = 222GPa + (93GPa - 222GPa)/\left(1 + e^{\frac{x-1.5\mu m}{0.4\mu m}}\right)$; $M_f = 87GPa + (40GPa - 87GPa)/\left(1 + e^{\frac{x-3.8\mu m}{0.1\mu m}}\right)$.

transition from the fiber response to the matrix response emerges. Although the inflection points of the two fitted curves match with the grain size distribution parameters, the grain size distribution has no connection to the size of the transition zone. This is determined by the indentation diameter, progressively covering a greater portion of the opposite phase as it gets closer to the interface. To categorize the indentations into two groups, representing fiber-like and matrix-like responses, we calculated the loading pre-factor (C). Using this parameter, we effectively isolated the performed indentations into two distinct groups (see Fig. 5).

Matrix-like responses were displayed up to 2 μm inside the fiber, characterized by a C factor of 241 ± 66·10^{-6} mN/nm^2. On the other hand, fiber-like responses appeared also about 2 μm away from the fiber/matrix interface, characterized by a C factor of 24 ± 10·10^{-6} mN/nm^2, consistent with values reported by Guruprasad et al. for pitch-derived fiber [46]. The transition zone within ± 2 μm from the fiber/-matrix interface may be attributed to two main factors: (i) the jagged interfaces, it is unknow whether there are matrix edges beneath the fiber or vice versa, and (ii) the transverse matrix cracks, which can be situated at various positions relative to the indented UHTC surface. Moreover, the grain edges within the fiber may alter the alignment of the graphitic sheets and other microstructural parameters, such as the interlayer distance and amount of voids. This observation suggests that the effective fiber volumetric content is smaller than the actual content. In particular, the reduction in effective fiber diameter, from 10 μm to 6 μm, indicates a 64 % reduction in effective fiber volumetric content. This observation necessitates further investigation and may help explain the Young's modulus of 230 GPa observed in the unidirectional composites, despite using 45 vol% of fiber with a modulus of 780 GPa [37].

3.2.3. *Indentation properties of fibers and matrix*

All the indentation curves sorted into the two groups are showed in Fig. A1. When plotting the hardness and modulus values as a function of the tip position with respect to the fiber/matrix interface for each group (see Fig. 6), a consistent trend emerges.

Fibers. According to the fitted trend, the values of H and M of the fiber increase from 1.1 GPa to 2.3 GPa and from 40 GPa to 87 GPa, respectively, as the imprint moves from the core of the fiber to the fiber/matrix interface. The values of H and M attributed to the core of the fiber, namely 1.1 GPa and 44 GPa, respectively, were the least influenced by the presence of the matrix and can be regarded as representative values for the fiber. Notably, these values are much smaller than those reported in literature (7 GPa and 100–80 GPa, respectively) [46–49]. This difference should be attributed to the larger maximum indentation depth achieved during the test (ranging from 1290 nm to 2200 nm) compared to the range reported in the literature (from 50 nm to 160 nm). This extended range may have enhanced the buckling and sliding phenomena of graphene sheets [46–49] and could be influenced by fiber misalignment, as supported by the results reported by Guruprasad *et al.* [46]. These results showed a decrease in hardness from 1.7 to 1.2 GPa and indentation modulus from 42 to 12 GPa of pitch-derived carbon fibers as the indentation angle with respect to the fiber axis increased from 12° to 90°. The facile spread of the highly oriented graphitic layers during the indentation with the pyramidal tip may explain the absence of any residual mark, consistent with the absence of plastic deformation observed in the indentation curves (see curves D and E of Fig. 3). The elastic strain recovery capability of pitch-derived carbon fiber has been previously observed through 10 kg Vickers indentation [38] and cycled thermal dilatometric analysis [37]. Similar behavior has also been observed in flexural and tensile tests for similar composites [33,36]. These observations support the pitch-derived fiber's ability, when embedded in the dense UHTC matrix, to retain its elastic behavior. This is in contrast to the results obtained for pitch-derived fibers embedded in a polymer matrix, where they were more prone to plastic deformation, despite using smaller indentation depths [46]. This difference could be attributed to the presence of high level of residual compressive stress along the longitudinal axis of the fiber, which aids in the recovery of the graphitic sheets' arrangement before the indentation process.

Matrix. Regarding the matrix response, its H and M values decreased from 11.5 GPa to 3.2 GPa, and from 222 GPa to 93 GPa, respectively, as the imprint moved from the bulk of the matrix to the fiber/matrix interface. In this case, the highest H and M values, estimated using the fitting curves (11.5 GPa and 222 GPa, respectively), agree with the value obtained in a zone less affected by the presence of the fibers (i.e. highest values of tip position). However, these values estimated for the matrix are lower than those reported in literature for the bulk ZrB_2 [50–56]. This is somewhat expected, as fibers, which have low transverse stiffness, work similarly the porosity in bulk ceramics. Therefore, these values refer to the indentation properties of the entire matrix, which includes the fibers and a higher amount of remaining porosities and matrix cracks compared to the corresponding bulk UHT-ceramics. In fact, these results are more aligned with the findings of Shahedi Asl et al. who reported hardness values between 10 and 25 GPa for ZrB_2 doped with graphite nano-flakes [64]. The indentation size effect (ISE), which

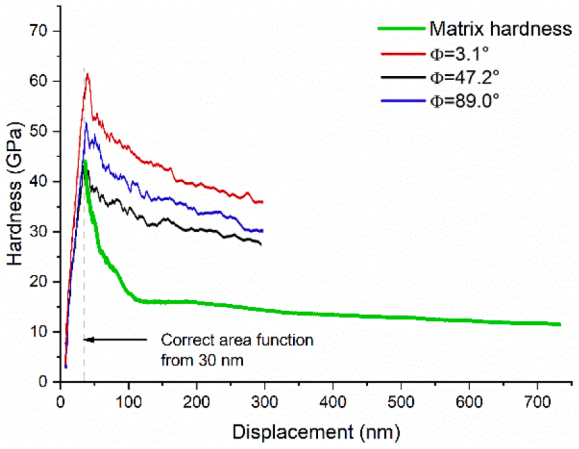

Fig. 7. Hardness vs. displacement of ZrB_2-based matrix (green solid line) and indentations (redrawn from Ref. [53]) corresponding to ZrB_2 grains with different crystal orientations: 3.1°, 47.2° and 89.0°. (For interpretation of the references to color in this figure legend, the reader is referred to the web version of this article).

entails a decrease in hardness with the increasing displacement, may have played a role in this phenomenon [53,65]. ISE is commonly attributed to several factors, including generation of dislocations, surface effects, cracking, surface contamination, among others. In case of UHTCMCs, it can be enhanced by the tensile residual stresses of the matrix that are not homogenously distributed. It is important to note that the initial hardness (about 45 GPa) is comparable to that of bulk ZrB_2, stabilizing within the range of 11.5–15 GPa after a displacement of 100 nm, corresponding to an imprint size smaller than 0.5 μm (see Fig. 7). This size is more comparable to the grain size rather than the distance to the nearest fiber, which is about 7 μm. This observation suggests that the lower H and M values of the matrix, in comparison to those of the corresponding bulk, result from the defectiveness of the matrix including pores and transverse cracks. The influence of the fiber became more noticeable only when the indentations were within approximately 2 μm of the matrix/fibers interface (as suggested by the inflection points reported in Fig. 6). Furthermore, the lower modulus of the matrix, compared to the corresponding monolithic ZrB_2 based ceramic, agree with that obtained through dilatometric analysis of 195 GPa [37].

3.2.4. *Energy-based analysis*

The results of energy-based analysis are presented in Fig. 8. In panel a, distinguishing between the values of total mechanical work (W_T, see Fig. 1) for fiber-like and matrix-like indentations proves challenging, particularly within the transition zone, where these values significantly overlap. However, with the aid of linear interpolation, it becomes evident that for matrix-like imprints W_T gradually decreases as the tip advances toward the bulk of the matrix. The distinction in behavior between fiber-like and matrix-like imprints becomes evident when considering the total energy constant, ν_T (Fig. 8b). Here, a value of $\nu_T = 1.72 \pm 0.24$ is clearly associated with fiber-like imprints, while matrix-like imprints exhibit a value of 1.18 ± 0.14. The higher value for fiber-like imprints indicated a less linear mechanical behavior of the fibers, primary due to buckling phenomena. The energy-based analysis revealed an increase in released elastic energy (W_E) when moving from the bulk of the matrix to the core of the fiber (Fig. 8c). Moreover, it is evident that the fiber-like indentations release a higher amount of W_E compared with the matrix-like ones (+32 %, see Table A1). Notably, both W_E and W_T, showed a gradual decrease as the tip moved toward the bulk of the matrix. This result can be attributed to the elastic extended behavior exhibited by the fibers, primarily due to the buckling of graphitic sheet. The occurrence of buckling in the graphitic sheets is also

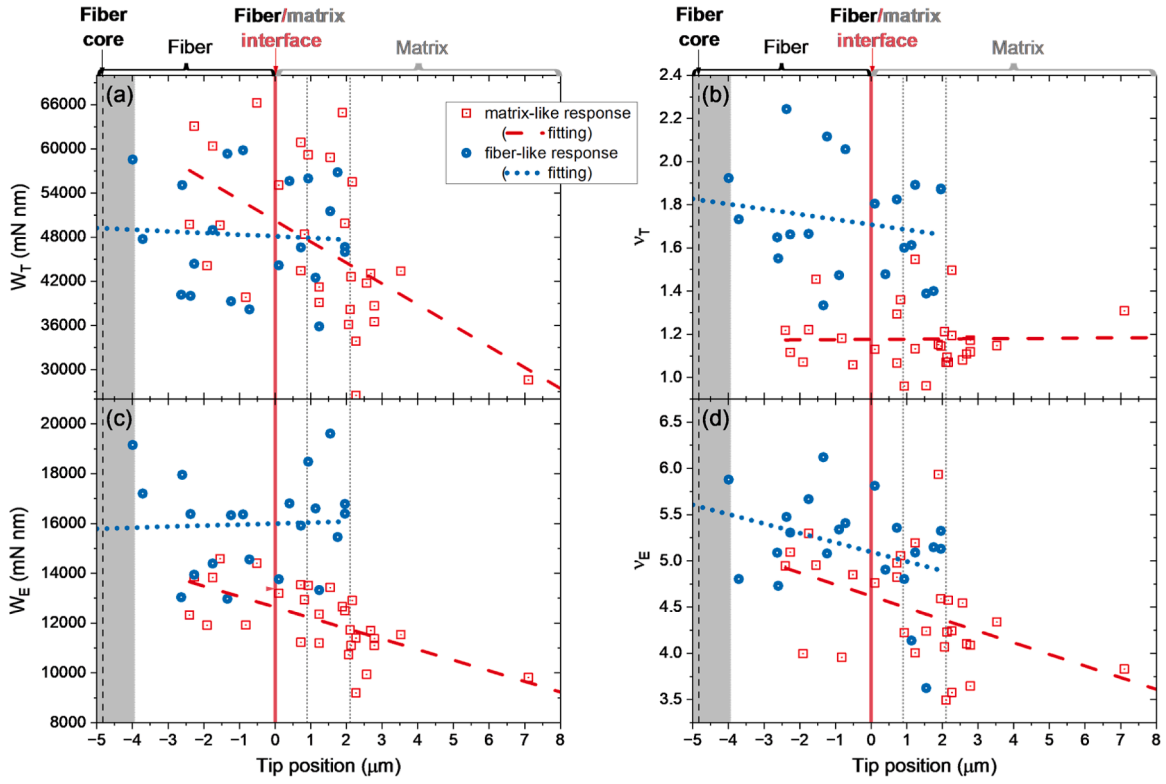

Fig. 8. (a) Total mechanical work during loading indentation step (W_T); (b) total energy constant (ν_T); (c) recovered elastic energy during unloading indentation step (W_E); and (d) elastic energy constant (ν_E) versus tip position with respect to the fiber/matrix interface (vertical red line at x = 0). The indentation results were grouped in two different ensembles: matrix- like response (square symbols) and fiber-like response (circle symbols).

evident during the loading step, where the energy accumulated through the buckling of these sheets is consistent with the high value of elastic energy released during the subsequent unloading step. Specifically, as said above, during the loading step, the fiber-like indentations display a lower total energy constant, indicating the spread from the fictitious absolute works due to easy deformation of the graphitic sheets as they buckle under extended displacements. These deformations of the graphitic sheets also affect the matrix-like imprints, as evidenced by the gradual decrease of the elastic energy constant (ν_E) from about 5.5–3.5 when moving from the core of the fiber toward the bulk of the matrix (Fig. 8d).

4. Conclusions

Micro-indentation tests at 100 mN allowed for the measurement of the hardness and indentation modulus of both ZrB_2-based matrix (11.5 GPa and 222 GPa, respectively) and pitch-derived carbon fibers (1.1 GPa and 40 GPa, respectively) within the unidirectional UHTCMC. These results agree with those reported in literature, taking into account the microstructural characteristics. Specifically, the lower indentation properties of the matrix, in comparison to the corresponding bulk ceramic, were attributed not only to the presence of fibers but, significantly, to the matrix's porosity and transverse cracks. The observed low hardness and modulus of the fibers were attributed to extended buckling and plastic sliding phenomena of graphene sheets. This effect was notably accentuated by the considerable indentation depth, which was an order of magnitude higher than what is typically reported in the literature, and by the compressive state of the fibers. The load-displacement curves were effectively categorized into two distinct response groups: matrix-like and fiber-like, based on the loading pre-factor parameter. This analysis revealed the presence of a transition zone extending beyond 2 μm into the other phase. This observation is significant as it supports the idea that the effective volumetric content of the fibers is lower than their actual content, probably due to the loss of the graphitic orientation in this region near the jagged interfaces. Notably, the pitch-derived fibers exhibited a remarkable ability to maintain their elastic behavior. This was evidenced by the absence of any residual imprint and the high amount of elastic energy released during the unloading step.

CRediT authorship contribution statement

P. Galizia: conceptualization, Methodology, Investigation, Validation, Formal analysis, Data curation, Visualization, Writing – original draft, Writing – review & editing. **S. Failla:** Resources. **C. Melandri:** Resources. **D. Sciti:** Project administration, Funding acquisition, Review .

Declaration of Competing Interest

The authors declare that they have no known competing financial interests or personal relationships that could have appeared to influence the work reported in this paper.

Acknowledgements

The research leading to these results has received funding from the European Union's Horizon 2020 Programme under grant agreement C^3HARME No. 685594.

Appendix A

All the indentation data collected for each indentation test are reported in Table A.1 where the values of the following parameters are reported: loading pre-factor (C), which allowed to isolate the performed indentations into two distinct groups: matrix-like response (first group reported in the following table) and fiber-like response (second group reported); distance between the center of indentation and the closest matrix/fiber interface (δ), this parameter was used to sort the indentation test within each group; maximum applied load (P_{max}); load value at which the increase in displacing ceases (P_L); penetration depth at which the increase in loading ceases (h_L); maximum displacement (h_{max}); contact depth (h_C); radius of the inscribed circle of the imprint ($r = h_{max} \cdot tan\ (65.3°)$); radius of the circumscribed circle of the imprint ($R = h_{max} \cdot tan\ (76.9°)$); contact area ($A_C$); stiffness (S); indentation modulus (M); indentation hardness (H); total mechanical work during loading step (W_T); recovered elastic energy during unloading step (W_E); total energy constant (ν_T) and elastic energy constant (ν_E).

Table A1
Collected data for each indentation test.

Test #	C 10^{-6} mN/nm^2	δ μm	P_{max} mN	P_L mN	h_L nm	h_{max} nm	h_C nm	r μm	R μm	A_C μm^2	S kN/m	M GPa	H GPa	W_T mN nm	W_P mN nm	W_E mN nm	ν_T	ν_E
9	309	7.1	102.2	101.8	732	739	616	1.6	3.2	8.8	619	221	11.6	28603	19456	9818	1.3088	3.8315
2	282	3.5	102.5	102.1	971	981	855	2.1	4.2	16.4	607	150	6.2	43384	32862	11534	1.1469	4.3398
20	198	2.8	102.8	101.6	882	894	759	1.9	3.8	13.1	573	160	7.8	38669	28759	11109	1.1720	4.0875
29	294	2.8	102.4	101.0	797	822	676	1.8	3.5	10.5	528	165	9.7	36496	27686	11379	1.1182	3.6471
39	281	2.7	102.3	101.9	933	943	808	2.1	4.1	14.7	565	147	6.9	43057	32373	11708	1.1085	4.1027
6	246	2.6	103.0	101.5	876	890	772	1.9	3.8	13.5	655	183	7.6	41737	33179	9939	1.0810	4.5432
11	238	2.3	102.6	100.1	773	780	665	1.7	3.4	10.2	669	222	10.1	26478	17994	9196	1.4971	4.2438
28	318	2.3	102.2	101.8	791	802	658	1.7	3.4	9.9	531	171	10.2	33866	23501	11405	1.1938	3.5756
34	183	2.2	103.0	101.4	1153	1164	1034	2.5	5.0	23.7	593	119	4.3	55478	43652	12908	1.0702	4.5730
7	245	2.1	102.7	102.2	909	919	790	2.0	3.9	14.1	593	159	7.2	42620	32587	11104	1.0944	4.2307
10	352	2.1	103.0	101.6	793	807	666	1.8	3.5	10.2	549	176	10.1	38161	27873	11726	1.0702	3.4938
41	320	2.1	102.3	101.2	856	863	728	1.9	3.7	12.1	568	166	8.5	36112	26140	10735	1.2118	4.0694
50	308	2.0	102.8	101.3	1111	1132	997	2.5	4.9	22.1	572	75	4.6	49855	39453	12496	1.1458	4.5894
4	192	1.9	102.5	102.0	1461	1473	1350	3.2	6.3	39.7	623	119	2.6	64929	53418	12657	1.1530	5.9345
38	310	1.5	102.1	100.7	1108	1131	987	2.5	4.9	21.6	531	95	4.7	58842	47786	13430	0.9610	4.2381
45	223	1.2	102.5	102.5	1244	1253	1144	2.7	5.4	28.8	707	111	3.6	41220	29771	12359	1.5467	5.1950
36	358	1.2	102.2	101.8	867	881	747	1.9	3.8	12.7	571	162	8.0	39128	29343	11198	1.1326	4.0041
31	257	0.9	102.1	100.6	1113	1134	994	2.5	4.9	22.0	548	114	4.6	59204	47838	13517	0.9597	4.2220
21	127	0.8	102.8	101.7	1279	1287	1164	2.8	5.5	29.8	627	112	3.4	48398	36239	12941	1.3593	5.0569
24	220	0.7	103.0	101.9	1261	1282	1137	2.8	5.5	28.5	534	96	3.6	60887	49490	13534	1.0670	4.8250

(*continued on next page*)

Table A1 (*continued*)

27	251	0.7	103.0	101.6	1091	1100	970	2.4	4.7	20.9	591	127	4.9	43432	33184	11227	1.2937	4.9763
15	178	0.1	102.9	102.2	1209	1229	1086	2.7	5.3	26.0	543	81	4.0	55061	43885	13195	1.1299	4.7607
16	149	-0.5	102.1	100.7	1373	1388	1256	3.0	6.0	34.5	569	103	2.9	66239	53340	14410	1.0589	4.8511
42	212	-0.8	102.6	102.1	917	924	784	2.0	4.0	13.9	547	93	7.3	39823	28558	11922	1.1816	3.9573
48	182	-1.5	102.8	102.0	1403	1417	1295	3.1	6.1	36.6	625	147	2.8	49591	36456	14586	1.4543	4.9541
22	143	-1.8	102.2	100.7	1443	1456	1332	3.2	6.3	38.7	612	99	2.6	60367	47830	13829	1.2211	5.2974
44	284	-1.9	102.7	102.3	920	931	792	2.0	4.0	14.2	553	94	7.2	44119	33246	11912	1.0716	3.9954
23	143	-2.3	102.4	102.0	1375	1384	1253	3.0	5.9	34.4	585	147	3.0	63099	50137	13853	1.1161	5.0941
47	185	-2.4	102.8	102.7	1179	1186	1062	2.6	5.1	24.9	619	96	4.1	49733	38172	12323	1.2179	4.9460
Mean	241	1.2	102.6	101.6	1063	1076	944	2.3	4.6	20.9	586	135	6.0	46848	36007	12136	1.1773	4.4702
Std. Dev.	65	2.0	0.3	0.6	222	223	225	0.5	1.0	9.5	44	39	2.7	10706	9788	1338	0.1407	0.5699
% COV	27	169	0.3	0.6	21	21	24	20	21	45	7	29	44	23	27	11	12	13
1	6	-4.0	102.5	102.1	2196	2205	2036	4.8	9.5	88.4	454	44	1.2	58532	40276	19149	1.9233	5.8791
25	42	-3.7	102.6	102.1	1612	1618	1489	3.5	7.0	48.0	594	81	2.1	47734	31148	17201	1.7322	4.8044
43	35	-2.6	103.1	102.6	1285	1293	1173	2.8	5.6	30.2	640	113	3.4	40156	27967	13039	1.6488	5.0888
5	17	-2.6	104.4	103.1	1638	1646	1489	3.6	7.1	48.0	492	67	2.1	55082	38039	17952	1.5514	4.7300
35	19	-2.4	102.6	102.1	1751	1756	1622	3.8	7.5	56.7	569	121	1.8	40021	24195	16381	2.2435	5.4757
30	26	-2.3	102.5	102.0	1440	1450	1321	3.2	6.2	38.0	595	71	2.7	44367	31398	13939	1.6630	5.3060
8	21	-1.8	103.0	102.6	1583	1590	1476	3.5	6.8	47.2	672	92	2.2	48980	35300	14390	1.6652	5.6680
19	4	-1.3	102.5	102.0	1545	1557	1423	3.4	6.7	44.0	574	94	2.3	59340	47595	12975	1.3335	6.1197
40	33	-1.2	102.3	101.9	1624	1629	1511	3.5	7.0	49.4	648	82	2.1	39265	23418	16334	2.1159	5.0802
3	23	-0.9	102.1	100.7	1726	1736	1585	3.8	7.5	54.2	506	88	1.9	59814	44402	16363	1.4737	5.3391
13	9	-0.7	102.6	102.6	1531	1535	1430	3.3	6.6	44.4	733	64	2.3	38173	24075	14557	2.0564	5.4084
18	30	0.1	102.1	101.7	1562	1574	1464	3.4	6.8	46.5	696	107	2.2	44159	31660	13766	1.8053	5.8119
49	23	0.4	102.7	102.2	1602	1612	1473	3.5	6.9	47.0	553	98	2.2	55634	39840	16805	1.4782	4.9037
32	23	0.7	103.0	103.0	1650	1655	1527	3.6	7.1	50.4	603	76	2	46595	31136	15914	1.8246	5.3565
33	21	0.9	102.9	101.5	1740	1750	1605	3.8	7.5	55.6	530	67	1.8	55958	38524	18486	1.6003	4.8032
46	32	1.1	102.8	102.3	1334	1343	1229	2.9	5.8	33.1	672	114	3.1	42493	26766	16605	1.6133	4.1381
12	24	1.2	103.0	102.6	1318	1323	1216	2.9	5.7	32.4	718	124	3.2	35858	23055	13327	1.8923	5.0903
26	37	1.5	102.7	101.3	1393	1403	1262	3.1	6.0	34.8	543	130	2.9	51531	33005	19608	1.3885	3.6242
37	38	1.8	102.4	101.9	1553	1561	1419	3.4	6.7	43.7	538	88	2.3	56793	42149	15456	1.3996	5.1470
17	17	2.0	102.7	102.3	1700	1706	1585	3.7	7.3	54.2	634	77	1.9	46666	30888	16398	1.8716	5.3234
14	26	2.0	103.0	102.6	1674	1679	1543	3.6	7.2	51.5	567	82	2.0	45980	29674	16785	1.8747	5.1288
Mean	24	-0.6	102.7	102.2	1593	1601	1470	3.5	6.9	47.5	597	90	2.27	48244	33072	15973	1.7217	5.1536
Std. Dev.	10	1.9	0.5	0.5	191	190	180	0.4	0.8	11.9	74	22	0.51	7407	6991	1900	0.2417	0.5488
% COV	42	-332	0.5	0.5	12	12	12	12	12	25	12	24	23	15	21	12	14	11
All tests	C	δ	P_{MAX}	P_L	h_L	h_{MAX}	h_C	r	R	A_C	S	M	H	W_T	W_P	W_E	ν_T	ν_E
	10^{-6} mN/nm^2	μm	mN	mN	nm	nm	nm	μm	μm	μm^2	kN/m	GPa	GPa	mN nm	mN nm	mN nm		
Mean	150	0.5	102.6	101.8	1286	1296	1165	2.8	5.6	32.1	591	116	4	47434	34774	13748	1.4060	4.7572
Std. Dev.	118	2.1	0.4	0.6	335	334	332	0.7	1.4	16.8	59	40	3	9486	8842	2478	0.3289	0.6547
% COV	79	470	0.4	0.6	26	26	29	25	26	53	10	34	62	20	25	18	23	14

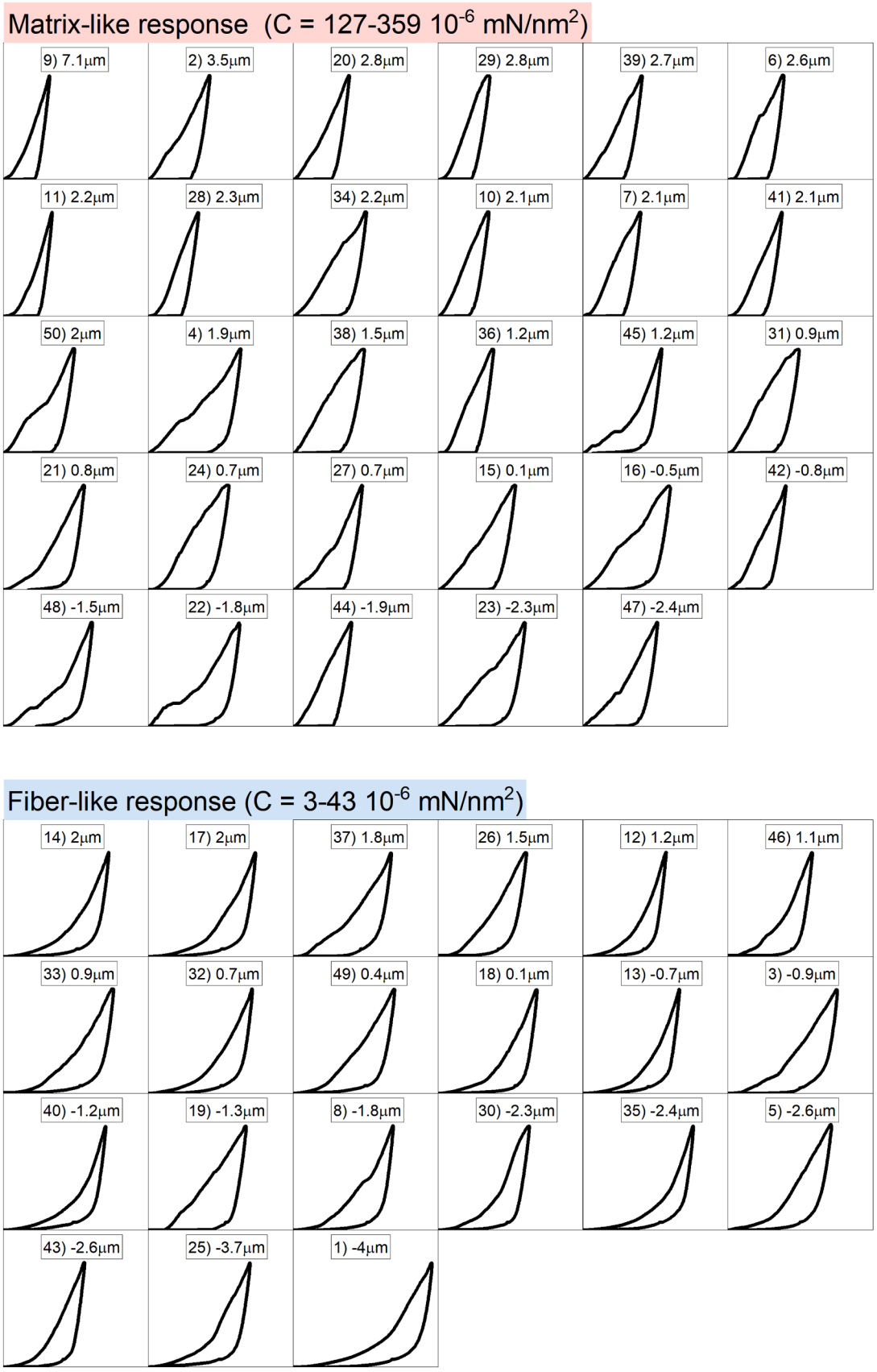

Fig. A1. All the indentation curves sorted as function of the tip position with respect to the matrix/fiber interface (the numbers in legends refer to number of indentation and the tip position with respect to the matrix/fiber interface). The indentation curves were grouped in matrix- and fiber-like response according to loading pre-factor (C). In all the graphs, the horizontal and vertical axes range from 0 to 2300 μm and 0–135 mN, respectively.

Appendix B. Supporting information

The indentation load-displacement curves for this article can be found in the online version at doi:10.1016/j.jeurceramsoc.2023.12.025.

References

[1] G. Karadimas, K. Salonitis, Ceramic matrix composites for aero engine applications & a review, Appl. Sci. 13 (2023) 3017, https://doi.org/10.3390/APP13053017.

[2] F.V. Harzand, S. Anzani, A. Babapoor, Recent advances in synthesis of ultra-high temperature ceramic matrix composites, Synth. Sinter. 2 (2022) 186–190, https://doi.org/10.53063/SYNSINT.2022.2475.

[3] D. Ni, Y. Cheng, J. Zhang, J.-X. Liu, J. Zou, B. Chen, H. Wu, H. Li, S. Dong, J. Han, X. Zhang, Q. Fu, G.-J. Zhang, Advances in ultra-high temperature ceramics, composites, and coatings, J. Adv. Ceram. 11 (2021) 1–56, https://doi.org/10.1007/S40145-021-0550-6.

[4] J. Binner, M. Porter, B. Baker, J. Zou, V. Venkatachalam, V.R. Diaz, A. D'Angio, P. Ramanujam, T. Zhang, T.S.R.C. Murthy, Selection, processing, properties and applications of ultra-high temperature ceramic matrix composites, UHTCMCs–a review, Int. Mater. Rev. 65 (2020) 389–444, https://doi.org/10.1080/09506608.2019.1652006.

[5] L.M. Rueschhoff, C.M. Carney, Z.D. Apostolov, M.K. Cinibulk, Processing of fiber-reinforced ultra-high temperature ceramic composites: a review, Int. J. Ceram. Eng. Sci. 2 (2020) 22–37, https://doi.org/10.1002/ces2.10033.

[6] Y. Arai, R. Inoue, K. Goto, Y. Kogo, Carbon fiber reinforced ultra-high temperature ceramic matrix composites: a review, Ceram. Int. 45 (2019) 14481–14489, https://doi.org/10.1016/J.CERAMINT.2019.05.065.

[7] S.R. Levine, E.J. Opila, M.C. Halbig, J.D. Kiser, M. Singh, J.A. Salem, Evaluation of ultra-high temperature ceramics foraeropropulsion use, J. Eur. Ceram. Soc. 22 (2002) 2757–2767, https://doi.org/10.1016/S0955-2219(02)00140-1.

[8] X. Jin, X. Fan, C. Lu, T. Wang, Advances in oxidation and ablation resistance of high and ultra-high temperature ceramics modified or coated carbon/carbon composites, J. Eur. Ceram. Soc. 38 (2017) 1–28, https://doi.org/10.1016/j.jeurceramsoc.2017.08.013.

[9] S. Tang, C. Hu, Design, preparation and properties of carbon fiber reinforced ultra-high temperature ceramic composites for aerospace applications: a review, J. Mater. Sci. Technol. 33 (2017) 117–130, https://doi.org/10.1016/j.jmst.2016.08.004.

[10] N.P. Padture, Advanced structural ceramics in aerospace propulsion, Nat. Mater. 15 (2016) 804–809, https://doi.org/10.1038/nmat4687.

[11] X. Li, Z. Guo, Q. Huang, C. Yuan, Research and application of biomimetic modified ceramics and ceramic composites: A review, J. Am. Ceram. Soc. (n.d.). https://doi.org/tps://doi.org/10.1111/jace.19490.

[12] V. Venkatachalam, S. Blem, A. Gülhan, J. Binner, Thermal qualification of the UHTCMCs produced using RF-CVI technique with VMK facility at DLR, J. Compos. Sci. 2022 6 (2022) 24, https://doi.org/10.3390/JCS6010024.

[13] S.R.C.M. Tammana, M. Duan, J. Zou, J. Wade, V. Venkatachalam, B. Baker, S. Nayebossadri, J. Binner, Ablation behaviour of Cf–ZrC-SiC with and without rare earth metal oxide dopants, Open Ceram. 10 (2022), 100270, https://doi.org/10.1016/J.OCERAM.2022.100270.

[14] P. Tatarko, F. Valenza, H. Ünsal, A. Kovalčíková, J. Sedláček, P. Šajgalík, Design of Lu_2O_3-reinforced Cf/SiC-ZrB_2-ZrC ultra-high temperature ceramic matrix composites: wetting and interfacial reactivity by $ZrSi_2$ based alloys, J. Eur. Ceram. Soc. (2020), https://doi.org/10.1016/j.jeurceramsoc.2020.05.055.

[15] V. Rubio, J. Binner, S. Cousinet, G. Le Page, T. Ackerman, A. Hussain, P. Brown, I. Dautremont, Materials characterisation and mechanical properties of Cf-UHTC powder composites, J. Eur. Ceram. Soc. 39 (2019) 813–824, https://doi.org/10.1016/j.jeurceramsoc.2018.12.043.

[16] B.J. Ackley, K.L. Martin, T.S. Key, C.M. Clarkson, J.J. Bowen, N.D. Posey, J. F. Ponder Jr, Z.D. Apostolov, M.K. Cinibulk, T.L. Pruyn, M. Dickerson, Advances in the synthesis of preceramic polymers for the formation of silicon-based and ultrahigh-temperature non-oxide ceramics, Chem. Rev. 123 (2023) 4188–4236, https://doi.org/10.1021/acs.chemrev.2c00381.

[17] X. Xu, X. Luan, J. Zhang, X. Cao, D. Zhao, L. Cheng, R. Riedel, Significant improvement of ultra-high temperature oxidation resistance of C/SiC composites upon matrix modification by SiHfBCN ceramics, Compos. Part B Eng. 253 (2023), 110553, https://doi.org/10.1016/J.COMPOSITESB.2023.110553.

[18] B.-W. Chen, D.-W. Ni, J. Lu, F.-Y. Cai, X.-G. Zou, Y.-D. Xue, H.-J. Zhou, Y.-S. Ding, S.-M. Dong, Microstructure and mechanical behaviors of 2D-Cf/ZrB_2-SiC composites at elevated temperatures, J. Eur. Ceram. Soc. (2022), https://doi.org/10.1016/J.JEURCERAMSOC.2022.05.063.

[19] P. Galizia, D. Sciti, N. Jain, Insight into microstructure and flexural strength of ultra-high temperature ceramics enriched SICARBON™ composite, Mater. Des. (2021), 109888, https://doi.org/10.1016/j.matdes.2021.109888.

[20] Y. Liu, Y. Cheng, D. Ma, N. Hu, W. Han, D. Liu, S. Wu, Y. An, A. Wang, Continuous carbon fiber reinforced ZrB_2-SiC composites fabricated by direct ink writing combined with low-temperature hot-pressing, J. Eur. Ceram. Soc. 42 (2022) 3699–3707, https://doi.org/10.1016/j.jeurceramsoc.2022.03.045.

[21] F. Servadei, L. Zoli, P. Galizia, C. Melandri, D. Sciti, Preparation of UHTCMCs by hybrid processes coupling polymer infiltration and pyrolysis with hot pressing and vice versa, J. Eur. Ceram. Soc. 42 (2022) 2118–2126, https://doi.org/10.1016/J.JEURCERAMSOC.2021.12.039.

[22] Y. Liu, Y. Zu, H. Tian, J. Dai, J. Sha, Microstructure and mechanical properties of continuous carbon fiber-reinforced ZrB_2-based composites via combined electrophoretic deposition and sintering, J. Eur. Ceram. Soc. 41 (2021) 1779–1787, https://doi.org/10.1016/j.jeurceramsoc.2020.10.044.

[23] D. Zhang, J. Feng, P. Hu, L. Xun, M. Liu, S. Dong, X. Zhang, Enhanced mechanical properties and thermal shock resistance of Cf/ZrB_2-SiC composite via an efficient slurry injection combined with vibration-assisted vacuum infiltration, J. Eur. Ceram. Soc. 40 (2020) 5059–5066, https://doi.org/10.1016/j.jeurceramsoc.2020.07.003.

[24] D. Zhang, P. Hu, S. Dong, X. Liu, C. Wang, Z. Zhang, X. Zhang, Oxidation behavior and ablation mechanism of Cf/ZrB_2-SiC composite fabricated by vibration-assisted slurry impregnation combined with low-temperature hot pressing, Corros. Sci. 161 (2019), 108181, https://doi.org/10.1016/j.corsci.2019.108181.

[25] H. Hu, Q. Wang, Z. Chen, C. Zhang, Y. Zhang, J. Wang, Preparation and characterization of C/SiC–ZrB_2 composites by precursor infiltration and pyrolysis process, Ceram. Int. 36 (2010) 1011–1016, https://doi.org/10.1016/j.ceramint.2009.11.015.

[26] P. Makurunje, S.C. Middleburgh, W.E. Lee, Addressing high processing temperatures in reactive melt infiltration for multiphase ceramic composites, J. Eur. Ceram. Soc. 43 (2023) 183–197, https://doi.org/10.1016/j.jeurceramsoc.2022.09.002.

[27] Z. Liu, Y. Wang, X. Xiong, H. Zhang, Z. Ye, Q. Long, Q. Wen, L. Wang, T. Li, C. Liu, Structural optimization and air-plasma ablation behaviors of C/C-SiC-(Zr_xHf_{1-x})C composites prepared by reactive melt infiltration method, Corros. Sci. 222 (2023), 111408, https://doi.org/10.1016/j.corsci.2023.111408.

[28] T. Marumo, N. Koide, Y. Arai, T. Nishimura, M. Hasegawa, R. Inoue, Characterization of carbon fiber-reinforced ultra-high temperature ceramic matrix composites fabricated via Zr-Ti alloy melt infiltration, J. Eur. Ceram. Soc. 42 (2022) 5208–5219, https://doi.org/10.1016/j.jeurceramsoc.2022.06.040.

[29] S. Chen, C. Zhang, Y. Zhang, H. Hu, Influence of pyrocarbon amount in C/C preform on the microstructure and properties of C/ZrC composites prepared via reactive melt infiltration, Mater. Des. 58 (2014) 570–576, https://doi.org/10.1016/j.matdes.2013.12.071.

[30] D. Sciti, L. Zoli, T. Reimer, A. Vinci, P. Galizia, A systematic approach for horizontal and vertical scale up of sintered ultra-high temperature ceramic matrix composites for aerospace – advances and perspectives, Compos. Part B Eng. 234 (2022), 109709, https://doi.org/10.1016/J.COMPOSITESB.2022.109709.

[31] Web Page of C3HARME, (n.d.). https://c3harme.eu/.

[32] D. Sciti, A. Vinci, L. Zoli, P. Galizia, S. Failla, S. Mungiguerra, G.D. Di Martino, A. Cecere, R. Savino, Propulsion tests on ultra-high-temperature ceramic matrix composites for reusable rocket nozzles, J. Adv. Ceram. 12 (2023) 1345–1360, https://doi.org/10.26599/JAC.2023.9220759.

[33] P. Galizia, D. Sciti, J. Binner, V. Venkatachalam, M.A. Lagos, F. Servadei, A. Vinci, L. Zoli, T. Reimer, Elevated temperature tensile and bending strength of ultra-high temperature ceramic matrix composites obtained by different processes, J. Eur. Ceram. Soc. 43 (2023) 4588–4601, https://doi.org/10.1016/j.jeurceramsoc.2023.03.055.

[34] P. Galizia, A. Vinci, L. Zoli, F. Monteverde, J. Binner, V. Venkatachalam, M. A. Lagos, T. Reimer, N. Jain, D. Sciti, Retained strength of UHTCMCs after oxidation at 2278 K, Compos. Part A Appl. Sci. Manuf. 149 (2021), 106523, https://doi.org/10.1016/j.compositesa.2021.106523.

[35] P. Galizia, S. Failla, L. Zoli, D. Sciti, Tough salami-inspired Cf/ZrB2 UHTCMCs produced by electrophoretic deposition, J. Eur. Ceram. Soc. 38 (2018) 403–409, https://doi.org/10.1016/j.jeurceramsoc.2017.09.047.

[36] P. Galizia, D. Sciti, Disclosing residual thermal stresses in UHT fibre-reinforced ceramic composites and their effect on mechanical behaviour and damage evolution, Compos. Part B Eng. 248 (2023), 110369, https://doi.org/10.1016/J.COMPOSITESB.2022.110369.

[37] P. Galizia, L. Zoli, D. Sciti, Impact of residual stress on thermal damage accumulation, and Young's modulus of fiber-reinforced ultra-high temperature ceramics, Mater. Des. 160 (2018) 803–809, https://doi.org/10.1016/J.MATDES.2018.10.019.

[38] P. Galizia, D. Sciti, F. Saraga, L. Zoli, Off-axis damage tolerance of fiber-reinforced composites for aerospace systems, J. Eur. Ceram. Soc. 40 (2020) 2691–2698, https://doi.org/10.1016/j.jeurceramsoc.2019.12.038.

[39] C. Sauder, J. Lamon, R. Pailler, The tensile behavior of carbon fibers at high temperatures up to 2400 °C, Carbon N.Y. 42 (2004) 715–725, https://doi.org/10.1016/j.carbon.2003.11.020.

[40] D. Sciti, L. Zoli, A. Vinci, L. Silvestroni, S. Mungiguerra, P. Galizia, Effect of PAN-based and pitch-based carbon fibres on microstructure and properties of continuous Cf/ZrB_2-SiC UHTCMCs, J. Eur. Ceram. Soc. 41 (2021) 3045–3050, https://doi.org/10.1016/j.jeurceramsoc.2020.05.032.

[41] M. Kharrat, A. Chateauminois, L. Carpentier, P. Kapsa, On the interfacial behaviour of a glass/epoxy composite during a micro-indentation test: assessment of interfacial shear strength using reduced indentation curves, Compos. Part A 28 (1997) 39–46, https://doi.org/10.1016/S1359-835X(96)00092-9.

[42] M. Zidi, L. Carpentier, A. Chateauminois, F. Sidoroff, Quantitative analysis of the micro-indentation behaviour of fibre-reinforced composites: development and validation of an analytical model, Compos. Sci. Technol. 60 (2000) 429–437, https://doi.org/10.1016/S0266-3538(99)00143-8.

[43] L. Zhang, C. Ren, C. Zhou, H. Xu, X. Jin, Single fiber push-out characterization of interfacial mechanical properties in unidirectional CVI-C/SiC composites by the nano-indentation technique, Appl. Surf. Sci. 357 (2015) 1427–1433, https://doi.org/10.1016/j.apsusc.2015.10.018.
[44] P. Diss, J. Lamon, L. Carpentier, J. Loubet, P. Kapsa, Sharp indentation behavior of carbon/carbon composites and varieties of carbon, Carbon N.Y. 40 (2002) 2567–2579, https://doi.org/10.1016/S0008-6223(02)00169-0.
[45] J.-M. Leyssale, G. Couégnat, S. Jouannigot, G.L. Vignoles, Mechanisms of elastic softening in highly anisotropic carbons under in-plane compression/indentation, Carbon N.Y. 197 (2022) 425–434, https://doi.org/10.1016/j.carbon.2022.06.063.
[46] T.S. Guruprasad, V. Keryvin, L. Charleux, J.P. Guin, O. Arnould, On the determination of the elastic constants of carbon fibres by nanoindentation tests, Carbon N.Y. 173 (2021) 572–586, https://doi.org/10.1016/J.CARBON.2020.09.052.
[47] S. Duan, F. Liu, T. Pettersson, C. Creighton, L.E. Asp, Determination of transverse and shear moduli of single carbon fibres, Carbon N.Y. 158 (2020) 772–782, https://doi.org/10.1016/j.carbon.2019.11.054.
[48] K. Shirasu, K. Goto, K. Naito, Microstructure-elastic property relationships in carbon fibers: A nanoindentation study, Compos. Part B Eng. 200 (2020), 108342, https://doi.org/10.1016/j.compositesb.2020.108342.
[49] T. Csanádi, D. Németh, C. Zhang, J. Dusza, Nanoindentation derived elastic constants of carbon fibres and their nanostructural based predictions, Carbon N. Y 119 (2017) 314–325, https://doi.org/10.1016/j.carbon.2017.04.048.
[50] M. Ivor, D. Medved, M. Vojtko, A. Naughton-Duszova, L. Marciniak, J. Dusza, Nanoindentation and tribology of ZrB_2 based luminescent ceramics, J. Eur. Ceram. Soc. 40 (2020) 4901–4908, https://doi.org/10.1016/j.jeurceramsoc.2020.03.021.
[51] T. Csanádi, M. Vojtko, R. Sedlák, A. Naughton-Duszová, Z. Pędzich, J. Dusza, Anisotropic dislocation nucleation in ZrB_2 grains and deformation behaviour of constituents of ZrB_2-SiC and ZrB_2-B_4C composites during nanoindentation, J. Eur. Ceram. Soc. 40 (2020) 2674–2682, https://doi.org/10.1016/j.jeurceramsoc.2019.12.024.
[52] T. Csanádi, A. Naughton-Duszová, J. Dusza, Anisotropic slip activation via homogeneous dislocation nucleation in ZrB_2 ceramic grains during nanoindentation - ScienceDirect, Scr. Mater. 152 (2018) 89–93, https://doi.org/10.1016/j.scriptamat.2018.04.025.
[53] T. Csanádi, A. Kovalčíková, J. Dusza, W.G. Farenholtz, G.E. Hilmas, Slip activation controlled nanohardness anisotropy of ZrB_2 ceramic grains, Acta Mater. 140 (2017) 452–464, https://doi.org/10.1016/j.actamat.2017.08.061.
[54] T. Csanádi, S. Grasso, A. Kovalčíková, J. Dusza, M.J. Reece, Nanohardness and elastic anisotropy of ZrB_2 crystals, J. Eur. Ceram. Soc. 36 (2016) 239–242, https://doi.org/10.1016/j.jeurceramsoc.2015.09.012.
[55] S. Guicciardi, C. Melandri, F.T. Monteverde, Characterization of pop-in phenomena and indentation modulus in a polycrystalline ZrB_2 ceramic, J. Eur. Ceram. Soc. 30 (2010) 1027–1034, https://doi.org/10.1016/j.jeurceramsoc.2009.10.014.
[56] E.J. Cheng, Y. Li, J. Sakamoto, S. Han, H. Sun, J. Noble, H. Katsui, G. Takashi, Mechanical properties of individual phases of ZrB_2-ZrC eutectic composite measured by nanoindentation, J. Eur. Ceram. Soc. 37 (2017) 4223–4227, https://doi.org/10.1016/j.jeurceramsoc.2017.05.031.
[57] L. Zoli, A. Vinci, P. Galizia, C. Melandri, D. Sciti, On the thermal shock resistance and mechanical properties of novel unidirectional UHTCMCs for extreme environments, Sci. Rep. 8 (2018), 9148, https://doi.org/10.1038/s41598-018-27328-x.
[58] V. Medri, C. Capiani, D. Gardini, Slip casting of ZrB_2–SiC composite aqueous suspensions, Adv. Eng. Mater. 12 (2010) 210–215, https://doi.org/10.1002/ADEM.200900275.
[59] W.C. Oliver, G.M. Pharr, Measurement of hardness and elastic modulus by instrumented indentation: advances in understanding and refinements to methodology, J. Mater. Res. 19 (2004) 3–20, https://doi.org/10.1557/JMR.2004.19.1.3.
[60] F. Sobhbidari, Q. Hu, Recent advances in the mechanical characterization of shales at nano-to micro-scales: a review, Mech. Mater. 162 (2021), 104043, https://doi.org/10.1016/J.MECHMAT.2021.104043.
[61] M.T. Attaf, New ceramics related investigation of the indentation energy concept, Mater. Lett. 57 (2003) 4684–4693, https://doi.org/10.1016/S0167-577X(03)00375-6.
[62] K.K. Jha, N. Suksawang, D. Lahiri, A. Agarwal, Energy-based analysis of nanoindentation curves for cementitious materials, Acids Mater. J. 109 (2012) 81–90, https://doi.org/10.14359/51683573.
[63] J. Wang, N. Salim, B. Fox, N. Stanford, Anisotropic compressive behaviour of turbostratic graphite in carbon fibre, Appl. Mater. Today 9 (2017) 196–203, https://doi.org/10.1016/j.apmt.2017.07.010.
[64] M. Shahedi Asl, B. Nayebi, A. Motallebzadeh, M. Shokouhimehr, Nanoindentation and nanostructural characterization of ZrB_2–SiC composite doped with graphite nano-flakes, Compos. Part B Eng. 175 (2019), 107153, https://doi.org/10.1016/j.compositesb.2019.107153.
[65] X. Jin, P. Li, C. Hou, X. Wang, X. Fan, C. Lu, G. Xiao, X. Shu, Oxidation behaviors of ZrB_2 based ultra-high temperature ceramics under compressive stress, Ceram. Int. 45 (2019) 7278–7285, https://doi.org/10.1016/j.ceramint.2019.01.009.